

## Article

# Crystal Growth and Thermal Properties of Quasi-One-Dimensional van der Waals Material $\text{ZrSe}_3$

Youming Xu , Shucheng Guo and Xi Chen \*

Department of Electrical and Computer Engineering, University of California, Riverside, CA 92521, USA

\* Correspondence: xichen@ucr.edu

**Abstract:**  $\text{ZrSe}_3$  with a quasi-one-dimensional (quasi-1D) crystal structure belongs to the transition metal trichalcogenides (TMTCs) family. Owing to its unique optical, electrical, and optoelectrical properties,  $\text{ZrSe}_3$  is promising for applications in field effect transistors, photodetectors, and thermoelectrics. Compared with extensive studies of the above-mentioned physical properties, the thermal properties of  $\text{ZrSe}_3$  have not been experimentally investigated. Here, we report the crystal growth and thermal and optical properties of  $\text{ZrSe}_3$ . Millimeter-sized single crystalline  $\text{ZrSe}_3$  flakes were prepared using a chemical vapor transport method. These flakes could be exfoliated into microribbons by liquid-phase exfoliation. The transmission electron microscope studies suggested that the obtained microribbons were single crystals along the chain axis.  $\text{ZrSe}_3$  exhibited a specific heat of  $0.311 \text{ J g}^{-1} \text{ K}^{-1}$  at 300 K, close to the calculated value of the Dulong–Petit limit. The fitting of low-temperature specific heat led to a Debye temperature of 110 K and an average sound velocity of  $2122 \text{ m s}^{-1}$ . The thermal conductivity of a polycrystalline  $\text{ZrSe}_3$  sample exhibited a maximum value of  $10.4 \pm 1.9 \text{ W m}^{-1} \text{ K}^{-1}$  at 40 K. The thermal conductivity decreased above 40 K and reached a room-temperature value of  $5.4 \pm 1.3 \text{ W m}^{-1} \text{ K}^{-1}$ . The Debye model fitting of the solid thermal conductivity agreed well with the experimental data below 200 K but showed a deviation at high temperatures, indicating that optical phonons could substantially contribute to thermal transport at high temperatures. The calculated phonon mean free path decreased with temperatures between 2 and 21 K. The mean free path at 2 K approached  $3 \text{ }\mu\text{m}$ , which was similar to the grain size of the polycrystalline sample. This work provides useful insights into the preparation and thermal properties of quasi-1D  $\text{ZrSe}_3$ .

**Keywords:** TMTCs;  $\text{ZrSe}_3$ ; quasi-1D materials; specific heat; thermal conductivity



**Citation:** Xu, Y.; Guo, S.; Chen, X.

Crystal Growth and Thermal Properties of Quasi-One-Dimensional van der Waals Material  $\text{ZrSe}_3$ .

*Micromachines* **2022**, *13*, 1994. <https://doi.org/10.3390/mi13111994>

Academic Editor: Hugo Aguas

Received: 16 October 2022

Accepted: 11 November 2022

Published: 17 November 2022

**Publisher's Note:** MDPI stays neutral with regard to jurisdictional claims in published maps and institutional affiliations.



**Copyright:** © 2022 by the authors. Licensee MDPI, Basel, Switzerland. This article is an open access article distributed under the terms and conditions of the Creative Commons Attribution (CC BY) license (<https://creativecommons.org/licenses/by/4.0/>).

## 1. Introduction

Transitional metal trichalcogenides (TMTCs) have attracted increasing research interest because of their unique quasi-one-dimensional (quasi-1D) crystal structures [1,2]. These materials contain two-dimensional (2D) layers, which are stacked in van der Waals (vdW) force between layers. In the 2D layers, they have stronger covalent bonding along one in-plane direction and weaker covalent bonding along the other. TMTCs have been extensively studied due to their interesting charge-density-wave (CDW) properties. The first discovery of CDW in TMTCs was reported in  $\text{NbSe}_3$  [3,4]. The phase transition occurred in  $\text{NbSe}_3$  was not accompanied by a structural transition, while a CDW formation was detected by electron diffraction. Afterward, CDW has been observed in  $\text{TiS}_3$  [5,6],  $\text{HfTe}_3$  [7], and  $\text{ZrTe}_3$  [8–11]. In addition to the CDW properties, TMTCs show other intriguing physical properties, such as superconductivity [12,13], optoelectronic behaviors [14–19], and thermoelectric properties [20–22].

Thermal transport properties are also important research topics for TMTCs. The single crystals of TMTCs exhibit anisotropic thermal transport properties due to their unique quasi-1D structures. Using a microthermal bridge method, Liu et al. discovered a high

thermal conductivity ( $\kappa$ ) along the chain axis in  $\text{TiS}_3$ , twice the value along the other in-plane direction at room temperature, with 66% of thermal conductivity contributed by highly dispersive optical phonons [23]. Such dispersive optical phonons in TMTCs and corresponding anisotropic thermal conductivity were also observed in  $\text{TaSe}_3$  and  $\text{ZrTe}_3$  by theoretical calculations [24]. Recently, Yang et al. observed superdiffusive phonon transport in  $\text{NbSe}_3$  nanowires, revealing that the thermal conductivity followed a  $1/3$  power law dependence of the sample length [25]. This finding was attributed to drastic elastic stiffening along the 1D chain direction. As a result, phonons along the chain direction dominated thermal transport.

$\text{ZrSe}_3$  is a semiconductor of the TMTC family, and it has a strong in-plane anisotropic structure.  $\text{ZrSe}_3$  crystallizes in the space group of  $P2_1/m$  (No. 11) and can be synthesized by chemical vapor transport (CVT) [26]. Patel et al. studied the electrical and optical properties of single-crystal  $\text{ZrSe}_3$  and found the direct and indirect bandgap of  $\text{ZrSe}_3$  to be 1.1 and 1.47 eV, respectively [27]. Electrical resistivity data both parallel and perpendicular to  $c$ -axis decreased with increasing temperature, confirming its semiconducting nature. Osada et al. utilized Raman scattering to investigate the layer-dependent phonon properties of  $\text{ZrSe}_3$  [28]. When the number of layers decreased, the phonon vibration mode  $A_g^3$ , which reflected a quasi-1D structure, experienced a considerable blueshift. Wang et al. studied the anisotropic optical and optoelectronic properties of  $\text{ZrSe}_3$ . The  $\text{ZrSe}_3$ -based photodetector showed a wide photoresponse range with photoresponsivity of  $11.9 \text{ mA W}^{-1}$  at 532 nm [29]. Li et al. studied the effect of uniaxial strain along different crystal directions in  $\text{ZrSe}_3$  and discovered a strongly anisotropic exciton peak shift [30]. When the sample was strained along the  $b$ -axis, the exciton peak shift was much larger than along the  $a$ -axis. The first-principles studies suggested that the deformation along the  $b$ -axis modified the electronic bands of more orbitals compared with the deformation along the  $a$ -axis. Zhu et al. studied spin-orbit torques in  $\text{ZrSe}_3$ /permalloy heterostructures [31]. When current was applied along the low-symmetry chain axis, an out-of-plane damping torque, corresponding to a large spin Hall conductivity, was detected in  $\text{ZrSe}_3$ . In addition to these experimental studies, a recent theoretical study suggested that a large thermoelectric figure of merit  $ZT$  of 2.4 at 800 K can be achieved in monolayer  $\text{ZrSe}_3$  [32].

Compared with the active studies on electrical, optical and optoelectronic properties, the thermal properties of  $\text{ZrSe}_3$  have rarely been reported. In this work, we investigated the crystal growth and optical and thermal properties of  $\text{ZrSe}_3$ . Millimeter-sized  $\text{ZrSe}_3$  single crystals were grown using the CVT method. These large crystals could be thinned down to microribbons by liquid-phase exfoliation. We further investigated the specific heat ( $C_p$ ) and thermal conductivity of polycrystalline  $\text{ZrSe}_3$  in the temperature range of 2–300 K. The analysis of specific heat data led to a Debye temperature of 110 K and an average sound velocity of  $2122 \text{ m s}^{-1}$ . The thermal conductivity of  $\text{ZrSe}_3$  reached a peak value of  $10.4 \pm 1.9 \text{ W m}^{-1} \text{ K}^{-1}$  at 40 K and a room-temperature value of  $5.4 \pm 1.3 \text{ W m}^{-1} \text{ K}^{-1}$ . The thermal conductivity was fitted via a Debye model, and the high-temperature deviation could be attributed to the optical phonon contribution to thermal conductivity. The phonon mean free path (MFP) calculated from the measured thermal conductivity increased with decreasing temperature, and approached a value of  $3 \text{ }\mu\text{m}$  at 2 K, which agreed well with the grain size of the polycrystalline sample.

## 2. Experimental Methods

### 2.1. Material Synthesis

The  $\text{ZrSe}_3$  crystals were synthesized via a CVT method [27]. The starting materials were zirconium powder (Zr, 100 mesh, purity >96%, Sigma Aldrich, Burlington, VT, USA), selenium powder (Se, 200 mesh, purity 99.999%, Alfa Aesar, Tewksbury, MA, USA), and iodine ( $\text{I}_2$ , flakes, purity 99.8%, Sigma Aldrich, Burlington, VT, USA) as the transport agent. The Zr and Se powders with molar ratio of 1:3 were homogeneously mixed and sealed under vacuum in a closed quartz ampoule with an  $\text{I}_2$  concentration of 5 mg/mL. The ampoule was heated in a tube furnace at 1173 K for 120 h, followed by furnace cooling for

15 h. The as-synthesized product was shiny silver flakes. A dense  $\text{ZrSe}_3$  pellet for thermal property measurements was prepared by grinding the  $\text{ZrSe}_3$  crystals and cold-pressing the powder under 63 MPa at room temperature, followed by annealing at 1173 K for 24 h in a vacuum-sealed quartz tube. The liquid-phase exfoliation was performed by sonicating the  $\text{ZrSe}_3$  crystals in acetone for 4 h.

## 2.2. Material Characterization

The purity and crystal structure of the samples were characterized by a PANalytical Empyrean Series 2 powder X-ray diffraction (XRD) diffractometer (Malvern Panalytical, Malvern, UK) with a  $\text{Cu K}\alpha$  source ( $\lambda = 1.54 \text{ \AA}$ ). The morphology of the samples was observed by a TESCAN Vega3 SBH scanning electron microscope (SEM) (TESCAN, Brno, Czech Republic) and a ThermoFisher Scientific Talos L120C transmission electron microscope (TEM) (ThermoFisher Scientific, Waltham, MA, USA). The pellet sample was cut into a typical dimension of  $0.5 \times 0.5 \times 6 \text{ mm}$  for the thermal conductivity measurement. The density ( $\rho$ ) of the pellet sample was determined to be  $4.27 \text{ g cm}^{-3}$ . A Quantum Design Physical Property Measurement System (PPMS) (Quantum Design, San Diego, CA, USA) was employed to measure the thermal conductivity along the direction perpendicular to the cold-pressing direction. The specific heat of the sample from 2 to 300 K was measured with the PPMS. The room-temperature Raman measurement was carried out with a HORIBA LabRam (HORIBA, Kyoto, Japan) using a 532 nm laser.

## 3. Results and Discussion

### 3.1. Phase and Microstructures

$\text{ZrSe}_3$  exhibits a quasi-1D crystal structure with a monoclinic  $\text{P2}_1/\text{m}$  space group (No. 11), as shown in Figure 1a. Each Zr atom is bonded to six Se atoms, forming an edge-sharing triangle prism along the  $b$ -axis (1D chains). The chains are stacked along the  $a$ -axis via a weaker covalent bond and form a 2D layer in the  $ab$  plane. The layers are further stacked by weak vdW forces along the  $c$ -axis. The room-temperature powder XRD pattern of  $\text{ZrSe}_3$  (Figure 1b) is consistent with the previously reported results [33], indicating that the pure  $\text{ZrSe}_3$  phase was formed by CVT. The corresponding lattice parameters are  $a = 5.415(7) \text{ \AA}$ ,  $b = 3.753(4) \text{ \AA}$ , and  $c = 9.473(8) \text{ \AA}$ , with  $\alpha = \gamma = 90^\circ$  and  $\beta = 97.72^\circ$ . In addition, a small amount of  $\text{ZrO}_2$  phase was observed, which could be attributed to the residual oxygen gas during the crystal growth.

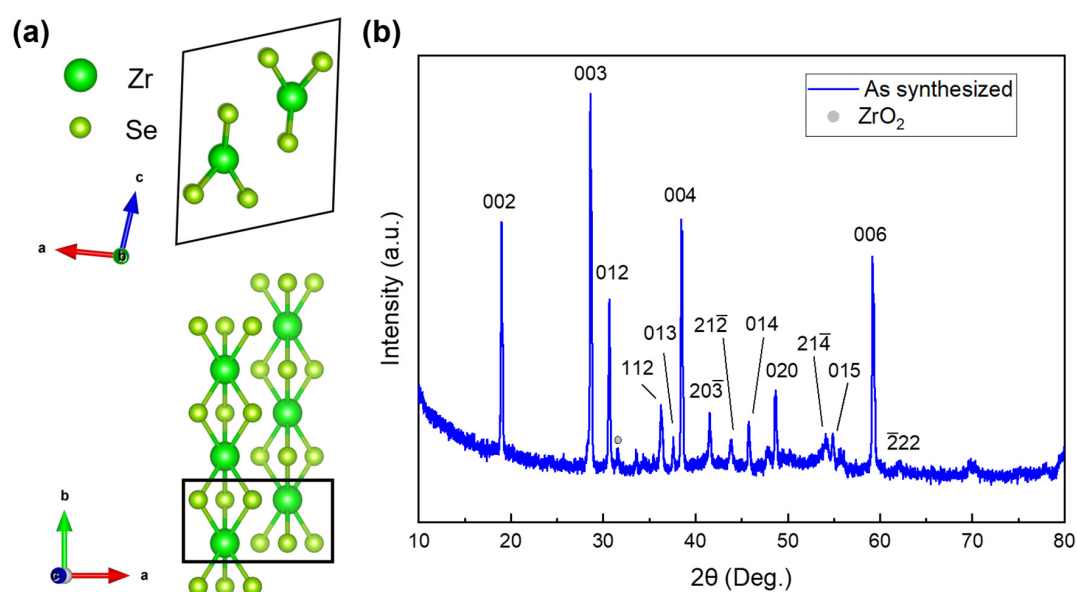


**Figure 1.** (a) Crystal structure of  $\text{ZrSe}_3$ . Each Zr atom bonds to six neighbor Se atoms, forming a triangular prism. (b) Indexed powder XRD pattern of the  $\text{ZrSe}_3$  sample.

Figure 2a,b show the SEM images of the as-synthesized  $\text{ZrSe}_3$  flakes. The lateral dimension of the flakes is about 1 mm. Microribbons with a width of about  $1\ \mu\text{m}$  could be observed at the edge of large flakes, as shown in Figure 2b. The quasi-1D microribbons are stacked in parallel, forming flat 2D layers through additional covalent Zr-Se bonding. The energy-dispersive spectroscopy (EDS) elemental mapping of constituent elements (Zr and Se) confirmed the chemical homogeneity of the flake, as displayed in Figure 2c. The quantitative EDS analysis was performed based on Zr  $L\alpha$  and Se  $L\alpha$  lines, and the stoichiometric ratio of Zr:Se was found to be approximately 1:2.9, indicating that a slight Se deficiency may have existed in the sample. The chalcogen element deficiency has also been reported in other quasi-1D transitional metal chalcogenides grown using the CVT method [34,35]. Further study is needed to quantify the Se vacancies in  $\text{ZrSe}_3$ .

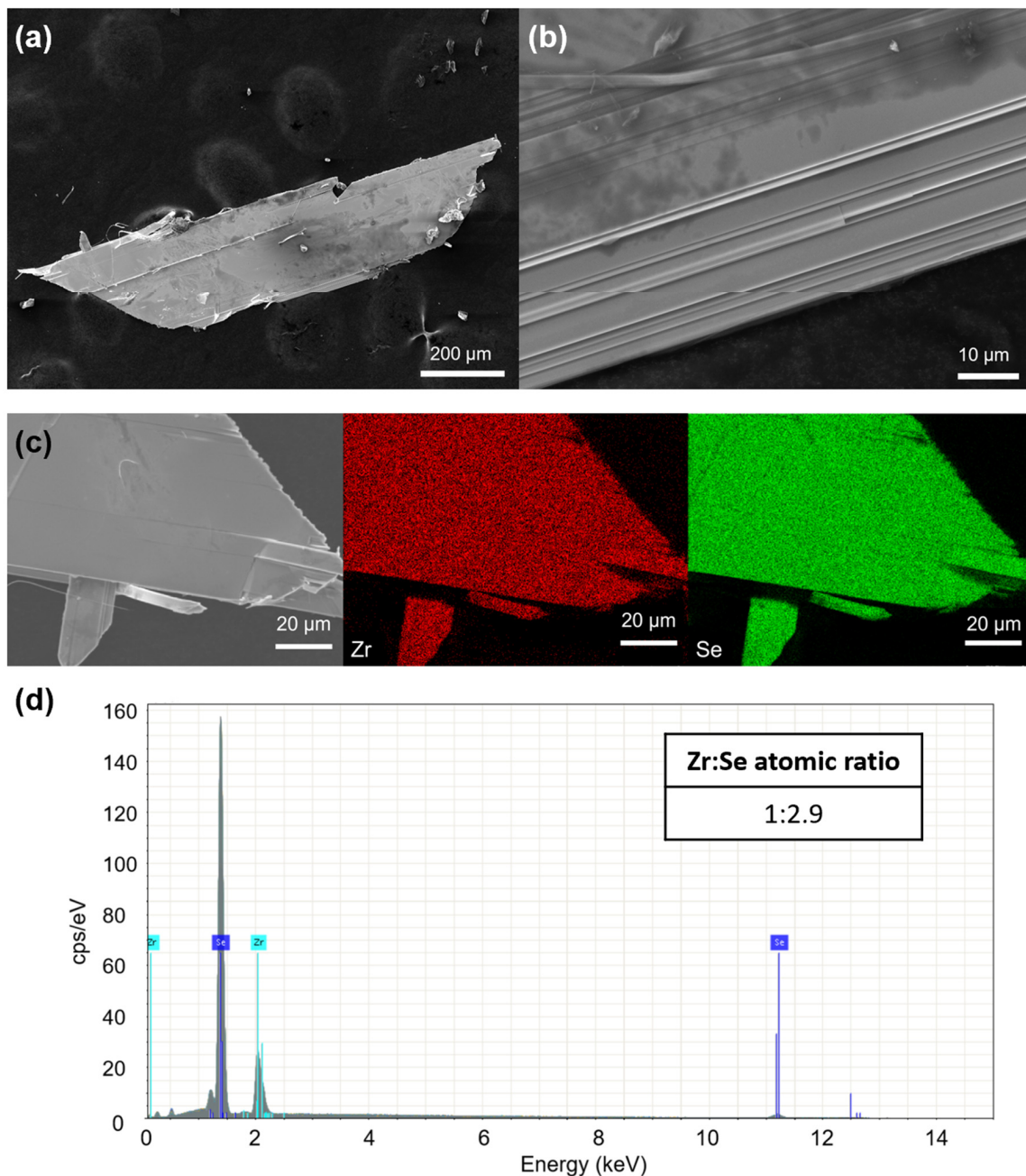


**Figure 2.** (a,b) SEM images of  $\text{ZrSe}_3$  after CVT. (c) EDS elemental mapping of Zr and Se in a  $\text{ZrSe}_3$  flake. (d) EDS spectrum of  $\text{ZrSe}_3$ .



Due to the small exfoliation energy of  $\text{ZrSe}_3$  monolayers ( $0.37 \text{ J m}^{-2}$ ) [36],  $\text{ZrSe}_3$  nanolayers were produced by mechanical exfoliation [30]. These findings motivated us to study the liquid-phase exfoliation of this compound. Figure 3a shows a typical microribbon of  $\text{ZrSe}_3$  with an in-plane dimension of  $20 \mu\text{m} \times 800 \text{ nm}$  after liquid-phase exfoliation. The thickness of the microribbon was estimated to be less than 200 nm, verifying the effectiveness of liquid exfoliation to produce  $\text{ZrSe}_3$  nanolayers. The selected area electron diffraction (SAED) pattern (Figure 3c) could be indexed along the  $[001]$  zone axis, confirming the microribbon was along the  $b$ -axis, which was the chain direction.

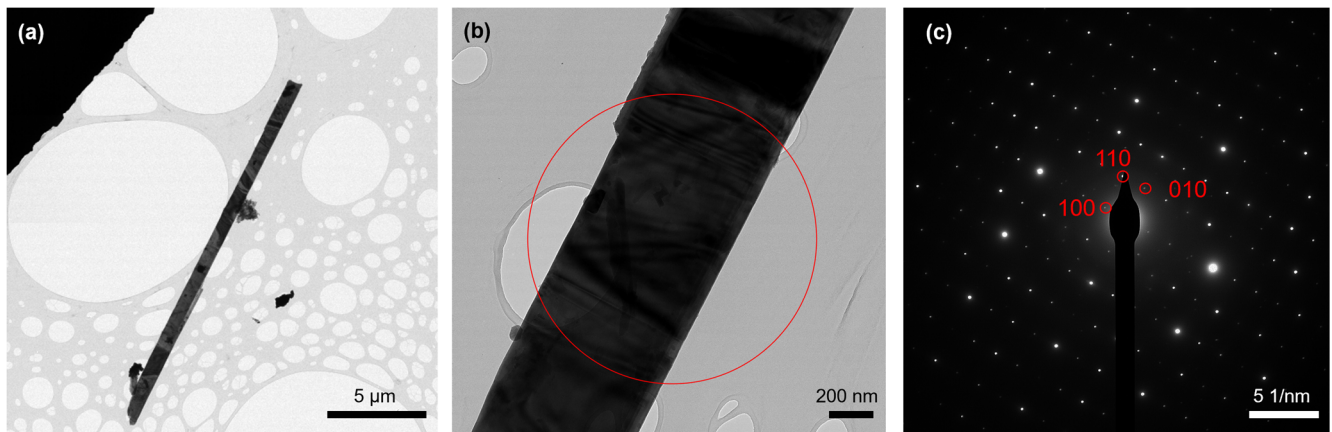


**Figure 3.** (a,b) TEM images of the  $\text{ZrSe}_3$  sample after liquid-phase exfoliation. The circle in (b) indicates the region for electron diffraction. (c) The corresponding SAED pattern obtained along  $[001]$  zone axis.

For the thermal property measurements, we prepared a polycrystalline  $\text{ZrSe}_3$  pellet by cold-pressing the CVT single crystals followed by annealing in a vacuum. Figure 4a shows the SEM image of the fracture surface of the pellet sample after cold-pressing. Microribbons were randomly distributed within the bulk sample. The average grain size was found to be about  $4 \mu\text{m}$ . As shown in Figure 4b, no compositional change could be observed in the XRD pattern of the sample after annealing in a vacuum, indicating its chemical stability.

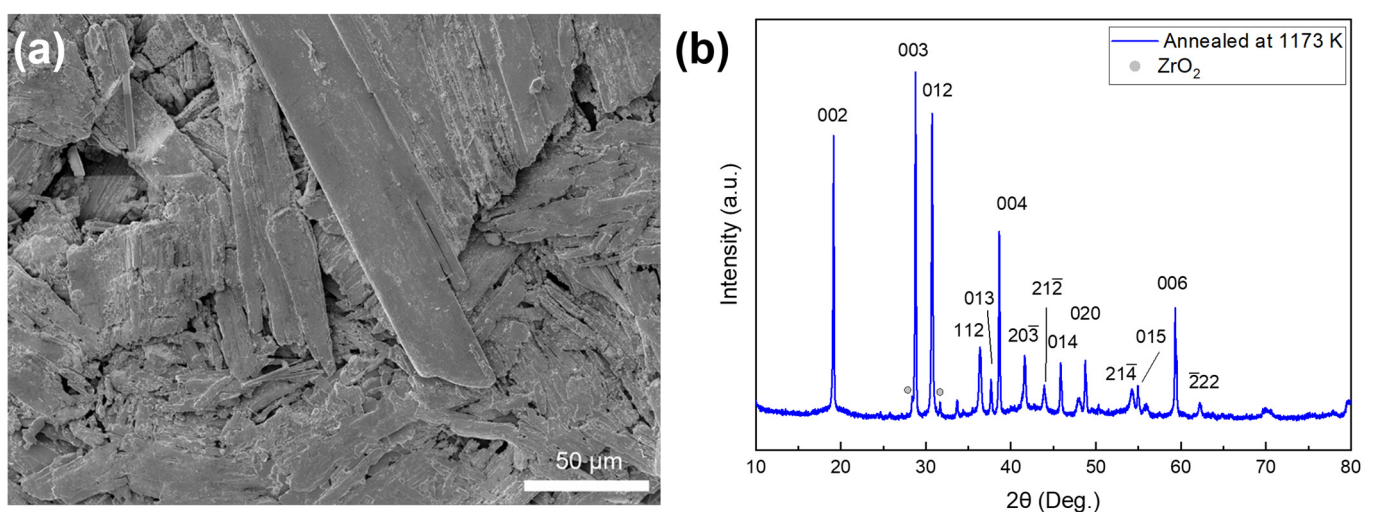


**Figure 4.** (a) SEM image of the  $\text{ZrSe}_3$  sample after cold-pressing showing the fracture surface perpendicular to the press direction. (b) Powder XRD pattern of  $\text{ZrSe}_3$  after annealing at 1173 K in vacuum.

### 3.2. Optical and Thermal Properties

The Raman spectrum of  $\text{ZrSe}_3$  at 300 K shows three characteristic peaks at 178, 235, and  $302\text{ cm}^{-1}$  in Figure 5. According to a previous Raman study on bulk  $\text{ZrSe}_3$ , three similar peaks at 178, 230, and  $300\text{ cm}^{-1}$  were also observed and were assigned to  $A_g^5$ ,  $A_g^6$ , and  $A_g^8$  vibration modes, respectively [28]. Among them,  $A_g^5$  and  $A_g^6$  vibration modes correspond to the out-of-plane vibrations, and  $A_g^8$  is due to the in-plane vibration mode. The  $A_g^5$  mode consists of the movement of both Zr and Se atoms in the quasi-1D chains, while the  $A_g^6$  and  $A_g^8$  modes only consist of the movement of Se atoms.

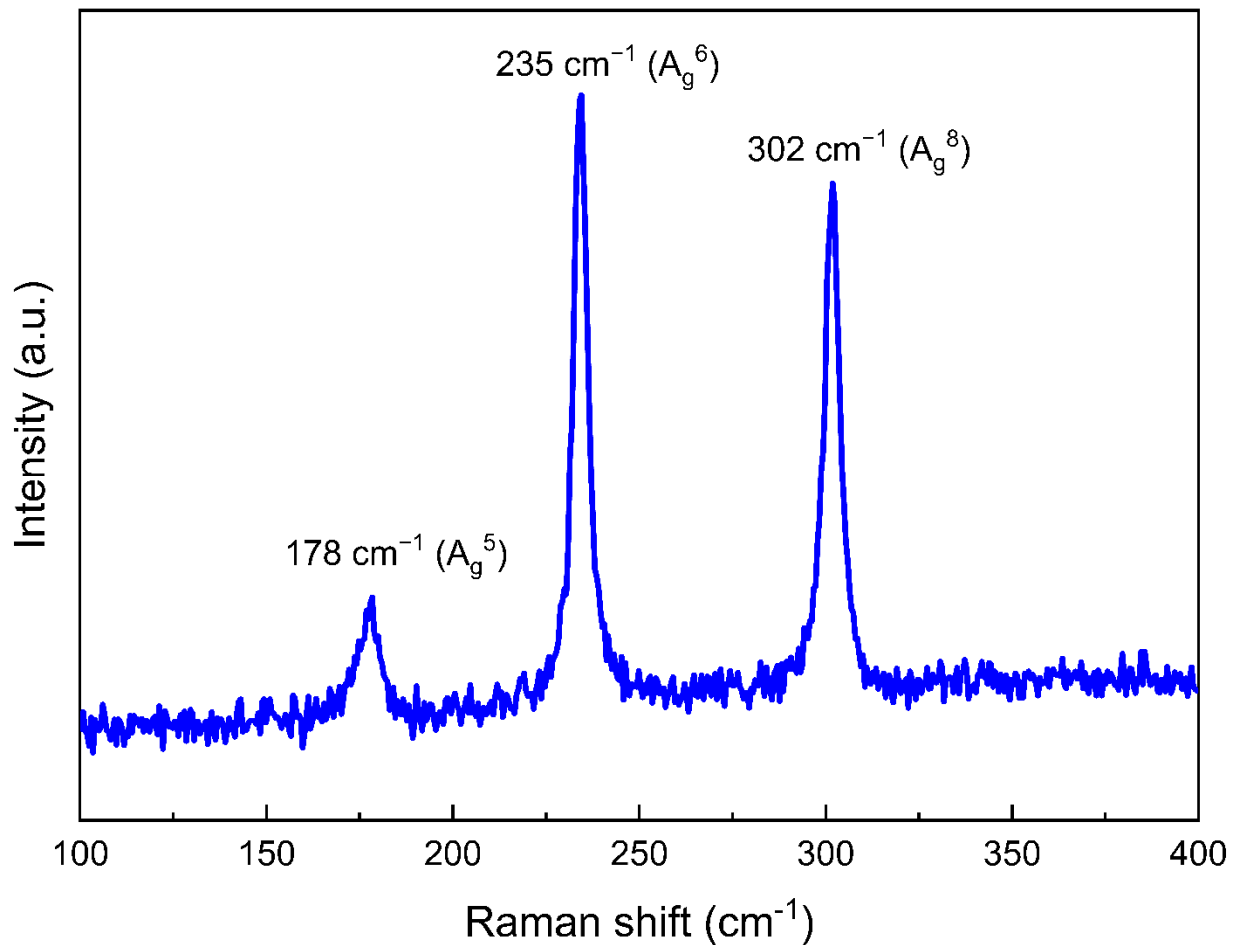


**Figure 5.** Raman spectrum of  $\text{ZrSe}_3$  at 300 K.

The specific heat of  $\text{ZrSe}_3$  from 2 to 300 K is shown in Figure 6a. The specific heat monotonically increased with temperature up to 300 K, and slightly exceeded the Dulong–Petit limit of  $0.304\text{ J g}^{-1}\text{ K}^{-1}$  above 280 K [37]. According to the Debye model [38], specific heat can be fitted via the following equation at low temperatures:

$$\frac{C_p}{T} = \gamma + \frac{12\pi^4 N k_B}{5\theta_D^3} T^2 \quad (1)$$

where  $\gamma$  is the electronic heat capacity coefficient,  $k_B$  is the Boltzmann constant,  $N$  is the number of atoms per mole,  $T$  is the temperature, and  $\theta_D$  is the Debye temperature.  $C_p/T$  versus  $T^2$  data below 9 K are shown in Figure 6b. The fitting led to a Debye temperature of 110 K with a sound velocity ( $v_s$ ) of  $2122\text{ m s}^{-1}$ , as listed in Table 1 together with other measured physical properties of  $\text{ZrSe}_3$ . The obtained data are in good agreement with those from a previous study on  $\text{ZrSe}_3$  [39], where the reported Debye temperature and

sound velocity were found to be 110 K and 2140 m s<sup>-1</sup>, respectively. The electronic heat capacity coefficient of ZrSe<sub>3</sub> is negligible, in agreement with its semiconductor nature.

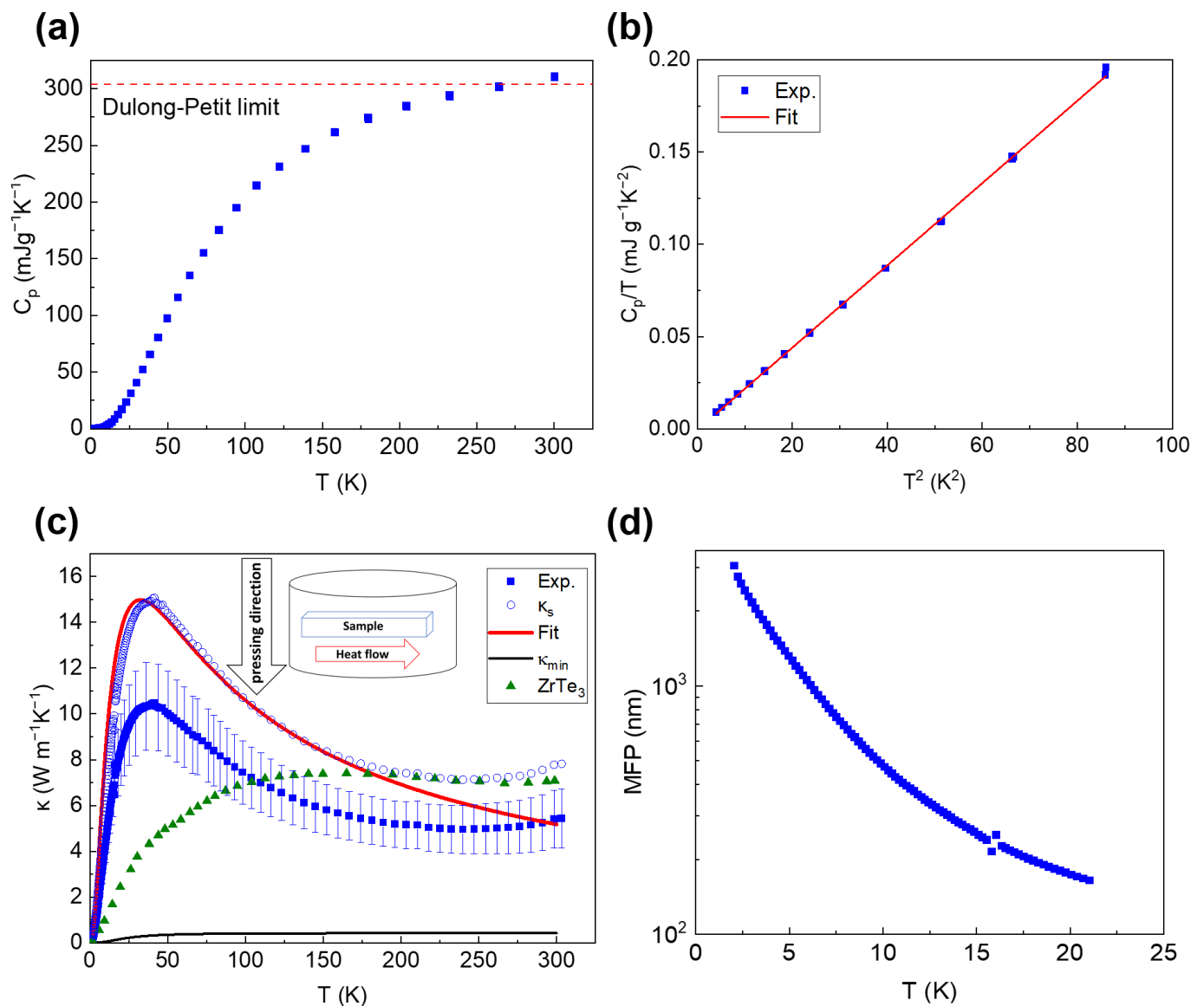


**Figure 6.** (a) Specific heat as a function of temperature for ZrSe<sub>3</sub>. The high-temperature limit was calculated using the Dulong–Petit law. (b)  $C_p/T$  versus  $T^2$  at low temperatures. (c) Thermal conductivity of ZrSe<sub>3</sub> as a function of temperature. The solid thermal conductivity was calculated by correcting the porosity effect. The experimental data for ZrTe<sub>3</sub> are included for comparison [40]. The solid thermal conductivity was fitted using the Debye model. The minimum thermal conductivity was calculated via the Cahill model [41]. The inset of (c) is a schematic illustration of the thermal conductivity measurement direction. Reprinted/adapted with permission from Ref. [40]. Copyright 2019, Elsevier. (d) Phonon MFP of the cold-pressed sample as a function of temperature below 21 K.

**Table 1.** Experimentally measured physical properties of ZrSe<sub>3</sub>.

Sample	$\rho$ (g cm <sup>-3</sup> )	$C_p$ (J g <sup>-1</sup> K <sup>-1</sup> )	$\theta_D$ (K)	$v_s$ (m s <sup>-1</sup> )	$\kappa$ (W m <sup>-1</sup> K <sup>-1</sup> )	$\kappa_{\max}$ (W m <sup>-1</sup> K <sup>-1</sup> )
ZrSe <sub>3</sub>	4.27	0.311 (300 K)	110	2122	5.4 ± 1.3 (300 K)	10.4 ± 1.9 (40 K)

Figure 6c shows the measured thermal conductivity of the cold-pressed ZrSe<sub>3</sub> sample in comparison with the data for a ZrTe<sub>3</sub> polycrystal [40]. ZrTe<sub>3</sub> has the same crystal

structure as  $\text{ZrSe}_3$  but with larger lattice parameters. The thermal conductivity of  $\text{ZrSe}_3$  shows a clear peak at 40 K, while the thermal conductivity of  $\text{ZrTe}_3$  exhibits a broad plateau in the temperature range of 120–300 K.  $\text{ZrSe}_3$  shows a stronger temperature dependence of thermal conductivity at low temperatures compared with  $\text{ZrTe}_3$ , indicating that the thermal conductivity of  $\text{ZrSe}_3$  is less affected by boundary scattering and defect scattering than  $\text{ZrTe}_3$ . The resistivity of the  $\text{ZrSe}_3$  polycrystalline sample exceeds the measurement limit of the PPMS. From a previous study, the resistivity of  $\text{ZrSe}_3$  single crystal was reported to be  $143.9 \, \Omega \, \text{cm}$  at room temperature [27]. According to the Wiedemann–Franz law, with a Lorentz number of  $2.44 \times 10^{-8} \, \text{V}^2 \, \text{K}^{-2}$ , the calculated electronic thermal conductivity ( $\kappa_E$ ) at 300 K is  $5.1 \times 10^{-6} \, \text{W} \, \text{m}^{-1} \, \text{K}^{-1}$ , which is negligible compared with lattice thermal conductivity ( $\kappa_L$ ).

At higher temperatures where phonon–phonon scattering dominates, the thermal conductivity of  $\text{ZrSe}_3$  is lower than that of  $\text{ZrTe}_3$ , with values of  $5.4 \, \text{W} \, \text{m}^{-1} \, \text{K}^{-1}$  and  $7 \, \text{W} \, \text{m}^{-1} \, \text{K}^{-1}$  at 300 K, respectively. However, because the Te atom is heavier than the Se atom, the phonon spectrum of  $\text{ZrTe}_3$  should be narrower than that of  $\text{ZrSe}_3$ , leading to smaller phonon velocities and stronger phonon–phonon scattering in  $\text{ZrTe}_3$ . Thus, the thermal conductivity of  $\text{ZrTe}_3$  should be lower than that of  $\text{ZrSe}_3$ , which seems to contradict our results. This discrepancy may have been caused by different synthesis parameters for the two samples, resulting in different porosities and texture effects. The calculated thermal conductivity of  $\text{ZrTe}_3$  along chain, cross-chain, and cross-plane directions are 9.6, 3.9, and  $2.3 \, \text{W} \, \text{m}^{-1} \, \text{K}^{-1}$  at 300 K, respectively [24]. The polycrystalline  $\text{ZrTe}_3$  was reported to have texture effects with preferred orientation along the chain axis [40], showing an experimental thermal conductivity close to the calculated value along the chain direction. In addition, a small amount of  $\text{ZrO}_2$ , observed by the XRD study, could enhance phonon scattering, and thus possibly decrease the thermal conductivity of  $\text{ZrSe}_3$ .

### 3.3. Thermal Transport Analysis

The Debye model was used to analyze the thermal transport in  $\text{ZrSe}_3$ . Before the Debye model fitting, the measured thermal conductivity needed to be corrected for porosity ( $f$ ) because the cold-pressed sample was not dense enough and contained voids, as can be seen from Figure 4a. The porosity of the sample can be calculated from the following equation

$$f = \left(1 - \frac{\rho}{\rho_{\text{theor}}}\right) \times 100\% \quad (2)$$

where  $\rho_{\text{theor}}$  is the theoretical density of  $\text{ZrSe}_3$ . The porosity of  $\text{ZrSe}_3$  was calculated to be 18%.

According to the effective medium theory [42], the solid thermal conductivity ( $\kappa_s$ ) is related to the measured thermal conductivity as

$$\kappa_s = \kappa \left(\frac{2 - 2f}{2 + 2f}\right)^{-1} \quad (3)$$

The obtained  $\kappa_s$  of  $\text{ZrSe}_3$  is presented in Figure 6c. We fit the solid thermal conductivity of  $\text{ZrSe}_3$  from 2 to 200 K using the following Debye model [43],

$$\kappa_s = \frac{k_B}{2\pi^2 v_s} \left(\frac{k_B T}{\hbar}\right)^3 \int_0^{\theta_D/T} \frac{x^4 e^x}{\tau_c^{-1}(e^x - 1)^2} dx, \quad (4)$$

where  $\hbar$  is the reduced Planck constant,  $x = \hbar\omega/k_B T$ ,  $\omega$  is phonon frequency, and  $\tau_c$  is the lattice relaxation rate. The lattice relaxation rate consists of boundary scattering ( $\tau_B$ ), point defect scattering ( $\tau_D$ ) and Umklapp scattering ( $\tau_U$ ) contributions and can be expressed as

$$\tau_c^{-1} = \tau_B^{-1} + \tau_D^{-1} + \tau_U^{-1} \quad (5)$$



The relaxation rates for boundary scattering, point defect scattering, and Umklapp scattering, respectively, are given by

$$\tau_B^{-1} = \frac{v_s}{L}, \quad \tau_D^{-1} = A\omega^4, \quad \tau_U^{-1} = B\omega^2 T e^{-\frac{\theta_D}{3T}} \quad (6)$$

where  $L$  is the average grain size; and  $A$  and  $B$  are prefactors for point defect scattering and Umklapp scattering, respectively. Figure 6c shows the results of fitting the thermal conductivity to the Debye model. The obtained fitting parameters were  $L = 5.0 \mu\text{m}$ ,  $A = 4.8 \times 10^{-42} \text{ s}^3$ , and  $B = 2.1 \times 10^{-18} \text{ s K}^{-1}$ . The obtained  $L$  value was consistent with the average grain size of about  $4 \mu\text{m}$  from the SEM study (Figure 4a).

Extrapolating the fitting toward  $T > 200 \text{ K}$  led to a deviation between the calculation and experimental data. Such a deviation could be attributed to the contribution of optical phonons to  $\kappa$ , which is not considered in the Debye model [44,45]. Debnath et al. calculated the phonon dispersion and thermal conductivity of  $\text{ZrTe}_3$  [24]. Several optical phonon modes were highly dispersive with large velocities. As a result, 33% of the lattice thermal conductivity was carried by optical phonons at room temperature. Similarly, Mortazavi et al. calculated the phonon dispersion of monolayer  $\text{ZrSe}_3$ , and dispersive optical modes were also shown in the phonon dispersion [36]. These theoretical results are consistent with our findings, suggesting that the optical phonons in  $\text{ZrSe}_3$  can also contribute to thermal transport substantially.

In order to better understand the phonon transport in polycrystalline  $\text{ZrSe}_3$ , acoustic phonon MFP can be calculated using the solid thermal conductivity as [46,47]

$$l = \kappa_s / \left[ \frac{k_B}{2\pi^2 v_s^2} \left( \frac{k_B T}{\hbar} \right)^3 \int_0^{\theta_D/T} \frac{x^4 e^x}{(e^x - 1)^2} dx \right] \quad (7)$$

The calculated MFP of  $\text{ZrSe}_3$  up to  $21 \text{ K}$  is shown in Figure 6d. As temperature decreases, the calculated acoustic phonon MFP increases and reaches  $3 \mu\text{m}$  at  $2 \text{ K}$ , consistent with the findings of the SEM study.

Furthermore, the minimum thermal conductivity ( $\kappa_{min}$ ) of  $\text{ZrSe}_3$  can be calculated according to the model developed by Cahill et al. [41] with the following equation:

$$\kappa_{min} = \left( \frac{\pi}{6} \right)^{1/3} k_B n_A^{2/3} v_s \left( \frac{T}{\theta_D} \right)^2 \int_0^{\theta_D/T} \frac{x^3 e^x}{(e^x - 1)^2} dx \quad (8)$$

where  $n_A$  is the density of atoms. The  $\kappa_{min}$  of  $\text{ZrSe}_3$  was found to be  $0.43 \text{ W m}^{-1} \text{ K}^{-1}$  at  $300 \text{ K}$ , which is less than one-tenth of the measured value. As such, it is expected that the thermal conductivity of  $\text{ZrSe}_3$  can be further suppressed by nanostructuring [48] or defect engineering [49] for thermoelectric applications.

#### 4. Conclusions

We report the crystal growth and thermal properties of quasi-1D vdW material  $\text{ZrSe}_3$ . Millimeter-sized  $\text{ZrSe}_3$  flakes were grown by the CVT method. Due to the weak vdW bond along the  $c$ -axis and relative weak covalent bond along the  $a$ -axis, the flakes could be exfoliated into microribbons using the liquid-phase exfoliation method. The cold-pressed  $\text{ZrSe}_3$  sample exhibited a maximum thermal conductivity of  $10.4 \pm 1.9 \text{ W m}^{-1} \text{ K}^{-1}$  at  $40 \text{ K}$  and a room-temperature value of  $5.4 \pm 1.3 \text{ W m}^{-1} \text{ K}^{-1}$ . The thermal transport analysis showed good agreement between the experimental data and Debye model fitting below  $200 \text{ K}$ , suggesting that the phonon transport in the polycrystalline sample was dominated by grain boundary, point defect, and Umklapp scattering. The high-temperature deviation between the fitting and experimental data could be attributed to the contribution of optical phonons. Combining the effective medium theory and Debye model, the acoustic phonon mean free path was calculated to be  $3 \mu\text{m}$  at  $2 \text{ K}$ , consistent with the SEM observation. In addition, the analysis of low-temperature specific heat led to a Debye temperature

of 110 K and an average sound velocity of  $2122 \text{ m s}^{-1}$ . This study provides the first experimental investigation of thermal transport in  $\text{ZrSe}_3$  as well as preparation of  $\text{ZrSe}_3$  nanostructures using liquid-phase exfoliation, which can enable novel applications based on quasi-1D  $\text{ZrSe}_3$ .

**Author Contributions:** Conceptualization, Y.X. and X.C.; methodology, Y.X. and S.G.; investigation, Y.X. and S.G.; writing—original draft preparation, Y.X.; writing—review and editing, Y.X., S.G. and X.C.; supervision, X.C.; project administration, X.C.; funding acquisition, X.C. All authors have read and agreed to the published version of the manuscript.

**Funding:** This work was supported by the National Science Foundation under Grant No. 2144328.

**Data Availability Statement:** The data presented in this study are available on request from the first author.

**Conflicts of Interest:** The authors declare no conflict of interest.

## References

- Balandin, A.A.; Kargar, F.; Salguero, T.T.; Lake, R.K. One-dimensional van der Waals quantum materials. *Mater. Today* **2022**, *55*, 74–91. [\[CrossRef\]](#)
- Island, J.O.; Molina-Mendoza, A.J.; Barawi, M.; Biele, R.; Flores, E.; Clamagirand, J.M.; Ares, J.R.; Sanchez, C.; van der Zant, H.S.J.; D’Agosta, R.; et al. Electronics and optoelectronics of quasi-1D layered transition metal trichalcogenides. *2D Mater.* **2017**, *4*, 022003. [\[CrossRef\]](#)
- Tsutsumi, K.; Takagaki, T.; Yamamoto, M.; Shiozaki, Y.; Ido, M.; Sambongi, T.; Yamaya, K.; Abe, Y. Direct Electron-Diffraction Evidence of Charge-Density-Wave Formation in  $\text{NbSe}_3$ . *Phys. Rev. Lett.* **1977**, *39*, 1675. [\[CrossRef\]](#)
- Hodeau, J.L.; Marezio, M.; Roucau, C.; Ayroles, R.; Meerschaut, A.; Rouxel, J.; Monceau, P. Charge-density waves in  $\text{NbSe}_3$  at 145K: Crystal structures, X-ray and electron diffraction studies. *J. Phys. C Solid State Phys.* **1978**, *11*, 4117–4134. [\[CrossRef\]](#)
- Gorlova, I.G.; Pokrovskii, V.Y. Collective conduction mechanism in a quasi-one-dimensional  $\text{TiS}_3$  compound. *Jetp. Lett.* **2009**, *90*, 295–298. [\[CrossRef\]](#)
- Huang, C.; Zhang, E.Z.; Yuan, X.; Wang, W.Y.; Liu, Y.W.; Zhang, C.; Ling, J.W.; Liu, S.S.; Xiu, F.X. Tunable charge density wave in  $\text{TiS}_3$  nanoribbons. *Chin. Phys. B* **2017**, *26*, 10. [\[CrossRef\]](#)
- Denholme, S.J.; Yukawa, A.; Tsumura, K.; Nagao, M.; Tamura, R.; Watauchi, S.; Tanaka, I.; Takayanagi, H.; Miyakawa, N. Coexistence of superconductivity and charge-density wave in the quasi-one-dimensional material  $\text{HfTe}_3$ . *Sci. Rep.* **2017**, *7*, 45217. [\[CrossRef\]](#) [\[PubMed\]](#)
- Hu, Y.W.; Zheng, F.P.; Ren, X.; Feng, J.; Li, Y. Charge density waves and phonon-electron coupling in  $\text{ZrTe}_3$ . *Phys. Rev. B* **2015**, *91*, 10. [\[CrossRef\]](#)
- Felser, C.; Finckh, E.W.; Kleinke, H.; Rocker, F.; Tremel, W. Electronic properties of  $\text{ZrTe}_3$ . *J. Mater. Chem.* **1998**, *8*, 1787–1798. [\[CrossRef\]](#)
- Hoesch, M.; Bosak, A.; Chernyshov, D.; Berger, H.; Krisch, M. Giant Kohn anomaly and the phase transition in charge density wave  $\text{ZrTe}_3$ . *Phys. Rev. Lett.* **2009**, *102*, 086402. [\[CrossRef\]](#)
- Liu, L.; Zhu, C.; Liu, Z.Y.; Deng, H.; Zhou, X.B.; Li, Y.; Sun, Y.; Huang, X.; Li, S.; Du, X.; et al. Thermal Dynamics of Charge Density Wave Pinning in  $\text{ZrTe}_3$ . *Phys. Rev. Lett.* **2021**, *126*, 256401. [\[CrossRef\]](#) [\[PubMed\]](#)
- Monceau, P.; Peyrard, J.; Richard, J.; Molinie, P. Superconductivity of Linear Trichalcogenide  $\text{NbSe}_3$  under Pressure. *Phys. Rev. Lett.* **1977**, *39*, 161–164. [\[CrossRef\]](#)
- Yue, B.; Zhong, W.; Deng, W.; Wen, T.; Wang, Y.; Yin, Y.; Shan, P.; Yu, X.; Hong, F. Insulator-to-superconductor transition in quasi-one-dimensional  $\text{HfS}_3$  under pressure. *arXiv* **2021**, arXiv:2111.02060.
- Mayorga-Martinez, C.C.; Sofer, Z.; Luxa, J.; Huber, S.; Sedmidubsky, D.; Brazda, P.; Palatinus, L.; Mikulics, M.; Lazar, P.; Medlin, R.; et al.  $\text{TaS}_3$  Nanofibers: Layered Trichalcogenide for High-Performance Electronic and Sensing Devices. *ACS Nano* **2018**, *12*, 464–473. [\[CrossRef\]](#)
- Xiong, W.W.; Chen, J.Q.; Wu, X.C.; Zhu, J.J. Individual  $\text{HfS}_3$  nanobelt for field-effect transistor and high performance visible-light detector. *J. Mater. Chem. C* **2014**, *2*, 7392–7395. [\[CrossRef\]](#)
- Dai, J.; Li, M.; Zeng, X.C. Group IVB transition metal trichalcogenides: A new class of 2D layered materials beyond graphene. *Wiley Interdiscip. Rev.-Comput. Mol. Sci.* **2016**, *6*, 211–222. [\[CrossRef\]](#)
- Dowben, P.A.; Binek, C.; Zhang, K.; Wang, L.; Mei, W.-N.; Bird, J.P.; Singisetti, U.; Hong, X.; Wang, K.L.; Nikonov, D. Towards a strong spin-orbit coupling magnetoelectric transistor. *IEEE J. Explor. Solid-State Comput. Devices Circuits* **2018**, *4*, 1–9. [\[CrossRef\]](#)
- Island, J.O.; Biele, R.; Barawi, M.; Clamagirand, J.M.; Ares, J.R.; Sanchez, C.; van der Zant, H.S.; Ferrer, I.J.; D’Agosta, R.; Castellanos-Gomez, A. Titanium trisulfide ( $\text{TiS}_3$ ): A 2D semiconductor with quasi-1D optical and electronic properties. *Sci. Rep.* **2016**, *6*, 22214. [\[CrossRef\]](#) [\[PubMed\]](#)
- Wang, J.; Jiang, C.Z.; Li, W.Q.; Xiao, X.H. Anisotropic Low-Dimensional Materials for Polarization-Sensitive Photodetectors: From Materials to Devices. *Adv. Opt. Mater.* **2022**, *10*, 2102436. [\[CrossRef\]](#)

20. Biele, R.; D'Agosta, R. Transport coefficients of layered  $\text{TiS}_3$ . *Phys. Rev. Mater.* **2022**, *6*, 8. [[CrossRef](#)]
21. Sakuma, T.; Nishino, S.; Miyata, M.; Koyano, M. Thermoelectric Properties for a Suspended Microribbon of Quasi-One-Dimensional  $\text{TiS}_3$ . *J. Electron. Mater.* **2018**, *47*, 3177–3183. [[CrossRef](#)]
22. Zhang, J.; Liu, X.; Wen, Y.; Shi, L.; Chen, R.; Liu, H.; Shan, B. Titanium Trisulfide Monolayer as a Potential Thermoelectric Material: A First-Principles-Based Boltzmann Transport Study. *ACS Appl. Mater. Interfaces* **2017**, *9*, 2509–2515. [[CrossRef](#)] [[PubMed](#)]
23. Liu, H.; Yu, X.; Wu, K.; Gao, Y.; Tongay, S.; Javey, A.; Chen, L.; Hong, J.; Wu, J. Extreme In-Plane Thermal Conductivity Anisotropy in Titanium Trisulfide Caused by Heat-Carrying Optical Phonons. *Nano Lett.* **2020**, *20*, 5221–5227. [[CrossRef](#)] [[PubMed](#)]
24. Debnath, T.; Debnath, B.; Lake, R.K. Thermal conductivity of the quasi-one-dimensional materials  $\text{TaSe}_3$  and  $\text{ZrTe}_3$ . *Phys. Rev. Mater.* **2021**, *5*, 034010. [[CrossRef](#)]
25. Yang, L.; Tao, Y.; Zhu, Y.; Akter, M.; Wang, K.; Pan, Z.; Zhao, Y.; Zhang, Q.; Xu, Y.Q.; Chen, R.; et al. Observation of superdiffusive phonon transport in aligned atomic chains. *Nat. Nanotechnol.* **2021**, *16*, 764–768. [[CrossRef](#)]
26. Kurita, S.; Tanaka, M.; Lévy, F. Optical spectra near the band edge of  $\text{ZrS}_3$  and  $\text{ZrSe}_3$ . *Phys. Rev. B* **1993**, *48*, 1356. [[CrossRef](#)]
27. Patel, K.; Prajapati, J.; Vaidya, R.; Patel, S.G. Optical and electrical properties of  $\text{ZrSe}_3$  single crystals grown by chemical vapour transport technique. *Bull. Mater. Sci.* **2005**, *28*, 405–410. [[CrossRef](#)]
28. Osada, K.; Bae, S.; Tanaka, M.; Raebiger, H.; Shudo, K.; Suzuki, T. Phonon Properties of Few-Layer Crystals of Quasi-One-Dimensional  $\text{ZrS}_3$  and  $\text{ZrSe}_3$ . *J. Phys. Chem. C* **2016**, *120*, 4653–4659. [[CrossRef](#)]
29. Wang, X.; Xiong, T.; Xin, K.; Yang, J.; Liu, Y.; Zhao, Z.; Liu, J.; Wei, Z. Polarization sensitive photodetector based on quasi-1D  $\text{ZrSe}_3$ . *J. Semicond.* **2022**, *43*, 102001. [[CrossRef](#)]
30. Li, H.; Sanchez-Santolino, G.; Puebla, S.; Frisenda, R.; Al-Enizi, A.M.; Nafady, A.; D'Agosta, R.; Castellanos-Gomez, A. Strongly Anisotropic Strain-Tunability of Excitons in Exfoliated  $\text{ZrSe}_3$ . *Adv. Mater.* **2022**, *34*, 2103571. [[CrossRef](#)]
31. Zhu, Y.H.; Chen, Q.; Wu, H.J.; Liang, J.; Tian, M.M.; Jiang, W.; Wang, J.C.; Li, R.X.; Li, S.K.; Huang, Z.C.; et al. Large spin hall conductivity in low-symmetry semiconductor  $\text{ZrSe}_3$ . *J. Alloys Compd.* **2022**, *918*, 165579. [[CrossRef](#)]
32. Zhou, Z.; Liu, H.; Fan, D.; Cao, G.; Sheng, C. High Thermoelectric Performance Originating from the Grooved Bands in the  $\text{ZrSe}_3$  Monolayer. *ACS Appl. Mater. Interfaces* **2018**, *10*, 37031–37037. [[CrossRef](#)]
33. Furuseth, S.; Brattås, L.; Kjekshus, A.; Andresen, A.F.; Fischer, P. On the Crystal Structures of  $\text{TiS}_3$ ,  $\text{ZrS}_3$ ,  $\text{ZrSe}_3$ ,  $\text{ZrTe}_3$ ,  $\text{HfS}_3$ , and  $\text{HfSe}_3$ . *Acta Chem. Scand.* **1975**, *29a*, 623–631. [[CrossRef](#)]
34. Barani, Z.; Kargar, F.; Ghafouri, Y.; Ghosh, S.; Godziszewski, K.; Baraghani, S.; Yashchyshyn, Y.; Cywiński, G.; Rumyantsev, S.; Salguero, T.T. Electrically Insulating Flexible Films with Quasi-1D Van Der Waals Fillers as Efficient Electromagnetic Shields in the GHz and Sub-THz Frequency Bands. *Adv. Mater.* **2021**, *33*, 2007286. [[CrossRef](#)] [[PubMed](#)]
35. Shahi, P.; Singh, D.J.; Sun, J.P.; Zhao, L.X.; Chen, G.F.; Lv, Y.Y.; Li, J.; Yan, J.Q.; Mandrus, D.G.; Cheng, J.G. Bipolar Conduction as the Possible Origin of the Electronic Transition in Pentatellurides: Metallic vs Semiconducting Behavior. *Phys. Rev. X* **2018**, *8*, 021055. [[CrossRef](#)]
36. Mortazavi, B.; Shojaei, F.; Yagmurcukardes, M.; Makaremi, M.; Zhuang, X.Y. A Theoretical Investigation on the Physical Properties of Zirconium Trichalcogenides,  $\text{ZrS}_3$ ,  $\text{ZrSe}_3$  and  $\text{ZrTe}_3$  Monolayers. *Energies* **2022**, *15*, 5479. [[CrossRef](#)]
37. Petit, A.; Dulong, P. Study on the measurement of specific heat of solids. *Ann. Chim. Phys.* **1819**, *10*, 395.
38. Debye, P. Zur Theorie der spezifischen Wärmen. *Ann. Der. Phys.* **1912**, *344*, 789–839. [[CrossRef](#)]
39. Provencher, R.; Ayache, C.; Jandl, S.; Jaygerin, J.P. Low-Temperature Specific-Heats of  $\text{ZrSe}_3$  and  $\text{ZrS}_3$ . *Solid State Commun.* **1986**, *59*, 553–556. [[CrossRef](#)]
40. Hooda, M.K.; Tripathi, T.S.; Yadav, C.S. Semiconducting nature and thermal transport studies of  $\text{ZrTe}_3$ . *J. Alloys Compd.* **2019**, *785*, 603–609. [[CrossRef](#)]
41. Cahill, D.G.; Watson, S.K.; Pohl, R.O. Lower limit to the thermal conductivity of disordered crystals. *Phys. Rev. B Condens. Matter.* **1992**, *46*, 6131–6140. [[CrossRef](#)] [[PubMed](#)]
42. Nan, C.-W.; Birringer, R.; Clarke, D.R.; Gleiter, H. Effective thermal conductivity of particulate composites with interfacial thermal resistance. *J. Appl. Phys.* **1997**, *81*, 6692–6699. [[CrossRef](#)]
43. Callaway, J. Model for Lattice Thermal Conductivity at Low Temperatures. *Phys. Rev.* **1959**, *113*, 1046–1051. [[CrossRef](#)]
44. Che, H.L.; Shi, J.; Wu, J.C.; Rao, X.; Liu, X.G.; Zhao, X.; Sun, X.F. Thermal conductivity of  $\text{Ca}_3\text{Co}_2\text{O}_6$  single crystals. *AIP Adv.* **2018**, *8*, 055811. [[CrossRef](#)]
45. Cheng, J.G.; Zhou, J.S.; Goodenough, J.B. Thermal conductivity, electron transport, and magnetic properties of single-crystal  $\text{Ca}_3\text{Co}_2\text{O}_6$ . *Phys. Rev. B* **2009**, *79*, 184414. [[CrossRef](#)]
46. Chen, X.; Weathers, A.; Moore, A.; Zhou, J.S.; Shi, L. Thermoelectric Properties of Cold-Pressed Higher Manganese Silicides for Waste Heat Recovery. *J. Electron. Mater.* **2012**, *41*, 1564–1572. [[CrossRef](#)]
47. Li, S.C.; Guo, S.C.; Xu, Y.M.; Zhou, J.S.; Chen, X. Role of Grain Size on Magnon and Phonon Thermal Transport in the Spin Ladder Compound  $\text{Ca}_9\text{La}_5\text{Cu}_{24}\text{O}_{41}$ . *Acs Appl. Electron. Mater.* **2022**, *4*, 787–794. [[CrossRef](#)]
48. Chen, X.; Shi, L.; Zhou, J.; Goodenough, J.B. Effects of ball milling on microstructures and thermoelectric properties of higher manganese silicides. *J. Alloys Compd.* **2015**, *641*, 30–36. [[CrossRef](#)]
49. Chen, X.; Girard, S.N.; Meng, F.; Lara-Curzio, E.; Jin, S.; Goodenough, J.B.; Zhou, J.; Shi, L. Approaching the Minimum Thermal Conductivity in Rhenium-Substituted Higher Manganese Silicides. *Adv. Energy Mater.* **2014**, *4*, 1400452. [[CrossRef](#)]